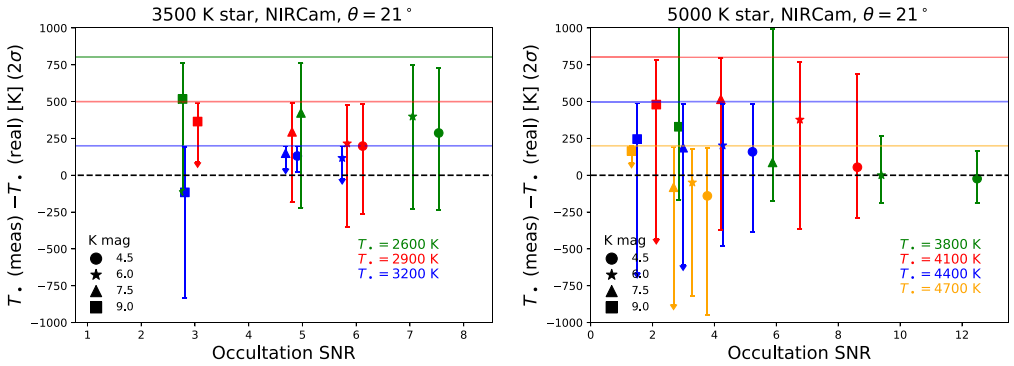

Figure 7. Same as Fig. 5 for spots at 21° stellar latitude, for the M (left) and K (right) scenarios observed by NIRCam/F150W2 + F322W2.

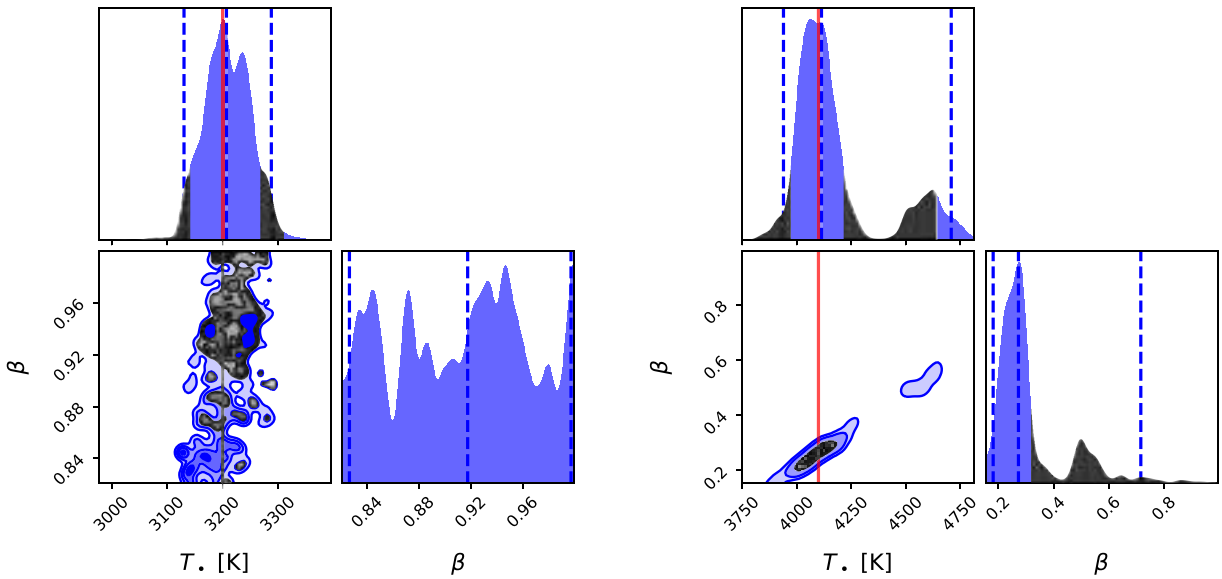

Figure 8. *Left:* $T_\bullet$ and β posterior distributions for the 14.5 *K* mag, M star observed with NIRSpec/Prism and a $T_\bullet = 3200$ K occulted starspot, with $\theta = 0°$. While the occultation signal is strong enough to exclude $T_\bullet = T_\star$, the high $\beta_{\rm min}$ forces the solution towards a warm spot (see Section 4.3). *Right:* $T_\bullet$ and β posterior distributions for the 7.5 *K* mag, K star observed with NIRCam/F150W2 + F322W2 and a $T_\bullet = 4100$ K occulted starspot, with $\theta = 0°$ (see Section 4.4). The 95 per cent credible intervals are represented with blue vertical dashed lines, while the true $T_\bullet$ value is indicated with a red vertical line.

distributions for all the simulations, for a more thorough examination of our results: in particular, we highlight that the bimodality just described is not found at the largest SNR values.

We remark that some arguments could be used to choose between the modes of the posteriors. For example, the lowest mode in Fig. 8, right-hand panel, has $\beta \equiv (R_{\rm p}/R_\bullet)^2 = (R_{\rm p}/R_\star)^2(R_\star/R_\bullet)^2 \simeq 0.5$. Using the measured transit depth value ($\simeq 0.01$), this means that the angular size of the starspot for this solution is $\simeq 8°$. Constraints on the largest likely value for the starspot size, which we do not examine here, could then be applied.

4.5 Implications of a single noise realization

To explore the consequences of using transits without Gaussian scatter for our simulations (Section 3.1), we selected a few scenarios resulting in significant constraints on $T_\bullet$, and repeated for ten times our simulations using each time a different noise realization. Here we discuss the case of the mag $K = 4.5$ K star with a 3800 K starspot and $\theta = 0°$, observed with NIRCam/F150W2 + F322W2. For each noise instance, we recorded the posterior distributions of $T_\bullet$ and β, and then compared the merged posterior distributions to those obtained without scatter in the transits.

Fig. 9 presents the posterior distributions derived with this method and the resulting 95 per cent percentiles. It can be noticed that, in most cases, the medians of the distributions are within each other's uncertainties; the median values themselves vary by no more than 10 per cent from one instance to the other, as well as compared to the case without Gaussian scatter. However, the merged posterior distribution shows – as expected – an increase in the uncertainties, which indicates that error bars drawn from a single noise instance are too optimistic. In this specific case, we observed a 20–30 K increase in the largest and lowest $T_\bullet$ values allowed within the 95 per cent percentiles. Hence, while one might be confident on the median $T_\bullet$ values achieved with the method we presented, the uncertainties should be regarded as likely underestimated in the mid- to high-SNR cases.

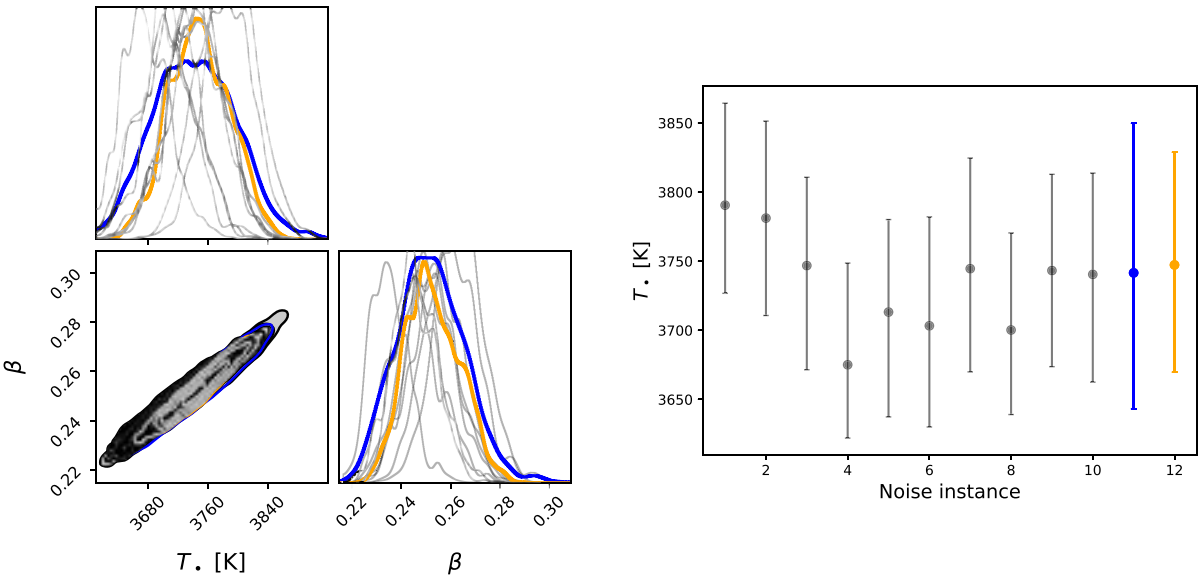

Figure 9. $T_\bullet - \beta$ posterior distributions (*left*) and $T_\bullet$ 95 per cent percentiles (*right*) derived from the transits without Gaussian scatter and with 10 noise realizations from one of our high-SNR simulations (see Section 4.5). Individual noise instances are marked in light grey, their merged distribution in blue (noise instance 11 in the right-hand panel), and the case without Gaussian scatter in orange (noise instance 12 in the right-hand panel).

5 DISCUSSION AND CONCLUSIONS

Our simulations show that *JWST* can be expected to be competitive for the determination of starspot temperatures from transit data with respect to *HST*. This latter was able to provide $\lesssim 250$ K uncertainties on starspots occulted by planets transiting very bright stars, such as the $\mathrm{mag}_K \simeq 5.5$ HD 189733, by using observations in the visible (Sing et al. 2011); about 400 K precision was also shown to be achievable, by stitching together visible and near-infrared spectra affected by unocculted spots (Bruno et al. 2020; Rathcke et al. 2021). The broad wavelength coverage of *JWST* will be able to place significant constraints by relying on near-infrared observations alone. Moreover, another advantage of *JWST* will be the ability to observe full transits without interruptions, thanks to its positioning in orbit around L2: this will allow a better coverage of transit events, both at the transit centre and edges.

With our method, we achieved $\lesssim 250$ K uncertainties on K and M stars with cool starspots observed with NIRCam/F150W2 + F322W2, as well as on $\mathrm{mag}_K \leq 12.5$ stars observed with NIRSpec/Prism. Large-contrast starspots highlight indeed important temperature-sensitive spectral features in the NIR (see Fig. 1). For this analysis, we exploited water and CO bands in the infrared, similarly to how visible-wavelength features such as TiO lines are used for earlier-type stars (e.g. Mirtorabi et al. 2003; O'Neal et al. 2004).

In this study, we adopted a single characteristic $\mu_\bullet$ value for both the occulted photosphere and the occulted active region. In reality, each occulted region encompasses a range of μ values. Using a single μ value should be a good approximation in most situations, given other uncertainties in the analysis. Nevertheless, in the case of giant starspots or starspot groups, this approximation might not be the most suitable.

Our study aims at assessing *JWST*'s capabilities in a wide range of observational settings and scenarios. In our formalism for modelling starspot occultations during transits, we simplified the transit 3D geometry in a 2D analytical formulation. This treatment is insensitive to the degeneracies between starspot size, location on stellar disc, and inclination of planetary orbit, but not on the correlation between $T_\bullet$ and the starspot size. Thanks to the width of the occultation bumps, we were however able to break the starspot temperature and size degeneracy in the largest SNR cases. We also remark that our formalism to derive starspot contrast spectra is valid as long as the planet disc is completely enclosed in the stellar disc. Its extension to the transit edges is beyond the scope of this paper.

The formalism we adopted for the determination of the starspot contrast from $T_\bullet$ requires the measurement of the transit depth (equation 8). In the first place, this means that the uncertainty on the results depends on the precision on the transit depth measure. Additionally, as atmospheric absorption by the planet can affect this quantity, our method can be directly applied to planets with a thin atmosphere, or with a flat transmission spectrum. In other cases, the transit depth variation due to the planet's atmosphere can be represented by a wavelength-dependent $\beta(\lambda)$ factor; alternatively, our model has to be combined with a transmission spectrum retrieval. This exploration requires a specific development, which is not the focus of this study.

To date, very few M-type transiting exoplanet host stars are known with $\mathrm{mag}_K < 8$.[3] However, the precision we achieved on starspot temperatures on M dwarfs with NIRCam/F150W2 + F322W2 is particularly relevant for measuring temperature contrasts for this stellar type, which are expected to be smaller than in FGK stars (Berdyugina 2005; Herbst et al. 2021). Our results are promising for large contrast cases, and could be extended to large starspots, which were observed both for M (Berdyugina 2011) and for K stars (e.g. Morris et al. 2017).

The simulations were performed for NIRSpec/Prism and NIRCam/F150W2 + F322W2, the modes that provide the broadest NIR wavelength coverage on *JWST*. With these configurations, valuable information on the activity level of stellar hosts will come for free in the case of a stellar active feature occultation. This will possibly act as an additional constraint on the level of contamination of planetary

[3] Source: exoplanet.eu.

transmission spectra: information on the average contrast of stellar active features could be used to determine the most suitable stellar models to be used in atmospheric retrievals (Iyer & Line 2020). Additional information could then be gained by combining this information with the output of ground-based photometric monitoring campaigns (e.g. Guilluy et al. 2020; Rosich et al. 2020).

In this work, we demonstrated the feasibility of constraining the temperature of occulted starspots with no additional observation other than those used to perform transmission spectroscopy. Despite the focus on *JWST*, the same method presented here could be used for any low-resolution facility working with transmission spectroscopy, such as the Atmospheric Remote-sensing Infrared Exoplanet Large-survey (*Ariel*; Tinetti et al. 2018). However, dedicated simulations should be used to model each instrument's properties.

ACKNOWLEDGEMENTS

GB acknowledges support from CHEOPS ASI-INAF agreement n. 2019-29-HH.0. GM and GC acknowledge the support of the ARIEL ASI-INAF agreement 2021-5-HH.0. This research has made use of the Spanish Virtual Observatory Filter Profile Service (http://svo2.cab.inta-csic.es/theory/fps/) supported from the Spanish MINECO through grant AYA2017-84089.

DATA AVAILABILITY

The specific intensity models used for this study can be downloaded from Zenodo (European Organization For Nuclear Research & OpenAIRE 2013), DOI 10.5281/zenodo.5609422 (https://zenodo.org/record/5609422) . The code underlying this article will be shared on reasonable request to the corresponding author. The throughput files used for our simulations can be downloaded from the SVO Filter Profile Service (https://jwst-docs.stsci.edu/near-infrared-camera/nircam-instrumentation/nircam-filters). Repositories for the software used in this study can be found in the referenced literature.

REFERENCES

Alam M. K. et al., 2018, AJ, 156, 298
Alonso R. et al., 2008, A&A, 482, L21
Ballerini P., Micela G., Lanza A. F., Pagano I., 2012, A&A, 539, A140
Balona L. A., Abedigamba O. P., 2016, MNRAS, 461, 497
Barros S. C. C., Boué G., Gibson N. P., Pollacco D. L., Santerne A., Keenan F. P., Skillen I., Street R. A., 2013, MNRAS, 430, 3032
Barstow J. K., Aigrain S., Irwin P. G. J., Kendrew S., Fletcher L. N., 2015, MNRAS, 448, 2546
Batalha N. E. et al., 2017, PASP, 129, 064501
Batalha N. E., Line M. R., 2017, AJ, 153, 151
Beaulieu J. P., Carey S., Ribas I., Tinetti G., 2008, ApJ, 677, 1343
Béky B., Kipping D. M., Holman M. J., 2014, MNRAS, 442, 3686
Berdyugina S. V., 2005, Living Rev. Sol. Phys., 2, 8
Berdyugina S. V., 2011, in Kuhn J. R., Harrington D. M., Lin H., Berdyugina S. V., Trujillo-Bueno J., Keil S. L., Rimmele T., eds, ASP Conf. Ser. Vol.437, Solar Polarization 6, Astron. Soc. Pac., San Francisco, p. 219
Bidaran B., Mirtorabi M. T., Azizi F., 2016, MNRAS, 457, 2043
Bruno G. et al., 2016, A&A, 595, A89
Bruno G. et al., 2018, AJ, 156, 124
Bruno G. et al., 2020, MNRAS, 491, 5361
Cracchiolo G., Micela G., Peres G., 2021, MNRAS, 501, 1733
Csizmadia S., Pasternacki T., Dreyer C., Cabrera J., Erikson A., Rauer H., 2013, A&A, 549, A9
Czesla S., Huber K. F., Wolter U., Schröter S., Schmitt J. H. M. M., 2009, A&A, 505, 1277
Désert J. M. et al., 2011, A&A, 526, A12
Dorren J. D., 1987, ApJ, 320, 756
Espinoza N., Fortney J. J., Miguel Y., Thorngren D., Murray-Clay R., 2017, ApJ, 838, L9
European Organization For Nuclear Research, OpenAIRE, 2013, Zenodo, CERN, Available at: https://www.zenodo.org/
Feng Y. K., Robinson T. D., Fortney J. J., Lupu R. E., Marley M. S., Lewis N. K., Macintosh B., Line M. R., 2018, AJ, 155, 200
Fraine J. et al., 2014, Nature, 513, 526
Gray D. F., 1976, The Observation and Analysis of Stellar Photospheres. Wiley, New York
Greene T. P., Line M. R., Montero C., Fortney J. J., Lustig-Yaeger J., Luther K., 2016, ApJ, 817, 17
Guilluy G. et al., 2020, A&A, 639, A49
Hauschildt P. H., Allard F., Baron E., 1999, ApJ, 512, 377
Heller R., 2019, A&A, 623, A137
Herbst K., Papaioannou A., Airapetian V. S., Atri D., 2021, ApJ, 907, 89
Higson E., Handley W., Hobson M., Lasenby A., 2019, Stat. Comput., 29, 891
Huber K. F., Czesla S., Wolter U., Schmitt J. H. M. M., 2010, A&A, 514, A39
Huitson C. M. et al., 2013, MNRAS, 434, 3252
Iyer A. R., Line M. R., 2020, ApJ, 889, 78
Jones H. R. A., Pavlenko Y., Viti S., Tennyson J., 2002, MNRAS, 330, 675
Keller C. U., Schüssler M., Vögler A., Zakharov V., 2004, ApJ, 607, L59
Kreidberg L., 2015, PASP, 127, 1161
Léger A. et al., 2009, A&A, 506, 287
Louden T., Wheatley P. J., Irwin P. G. J., Kirk J., Skillen I., 2017, MNRAS, 470, 742
Mancini L. et al., 2017, MNRAS, 465, 843
Mandal S., Hegde M., Samanta T., Hazra G., Banerjee D., Ravindra B., 2017, A&A, 601, A106
Mandel K., Agol E., 2002, ApJ, 580, L171
Marino G., Rodonó M., Leto G., Cutispoto G., 1999, A&A, 352, 189
Maxted P. F. L., 2018, A&A, 616, A39
McCullough P. R., Crouzet N., Deming D., Madhusudhan N., 2014, ApJ, 791, 55
McQuillan A., Mazeh T., Aigrain S., 2014, ApJS, 211, 24
Mirtorabi M. T., Wasatonic R., Guinan E. F., 2003, ApJ, 125, 3265
Montalto M., Boué G., Oshagh M., Boisse I., Bruno G., Santos N. C., 2014, MNRAS, 444, 1721
Morello G., Tsiaras A., Howarth I. D., Homeier D., 2017, AJ, 154, 111
Morris B. M., Hebb L., Davenport J. R. A., Rohn G., Hawley S. L., 2017, ApJ, 846, 99
Neff J. E., O'Neal D., Saar S. H., 1995, ApJ, 452, 879
Nielsen M. B., Gizon L., Cameron R. H., Miesch M., 2019, A&A, 622, A85
O'Neal D., Neff J. E., Saar S. H., Cuntz M., 2004, AJ, 128, 1802
Oshagh M., Santos N. C., Ehrenreich D., Haghighipour N., Figueira P., Santerne A., Montalto M., 2014, A&A, 568, A99
Panja M., Cameron R., Solanki S. K., 2020, ApJ, 893, 113
Pont F., Knutson H., Gilliland R. L., Moutou C., Charbonneau D., 2008, MNRAS, 385, 109
Pont F., Sing D. K., Gibson N. P., Aigrain S., Henry G., Husnoo N., 2013, MNRAS, 432, 2917
Pontoppidan K. M. et al., 2016, Proceedings of the SPIE, 9910, 15
Rackham B. et al., 2017, ApJ, 834, 151
Rackham B. V., Apai D., Giampapa M. S., 2018, ApJ, 853, 122
Rackham B. V., Apai D., Giampapa M. S., 2019, AJ, 157, 96
Ramsey L. W., Nations H. L., 1980, ApJ, 239, L121
Rathcke A. D. et al., 2021, AJ, 162, 138
Rauer H. et al., 2014, Exp. Astron., 38, 249
Ricker G. R. et al., 2014, Proceedings of the SPIE, 9143, 15
Rieke M. J., Kelly D., Horner S., 2005, in Heaney J. B., Burriesci L. G., eds, Proc. SPIE Conf. Ser. Vol. 5904, Cryogenic Optical Systems and Instruments XI, SPIE, Bellingham. p. 1

Rodrigo C., Solano E., Bayo A., 2012, SVO Filter Profile Service Version 1.0, IVOA Working Draft 15 October 2012, Available at:https://ui.adsabs.harvard.edu/abs/2012ivoa.rept.1015R
Rodrigo C., Solano E., 2020, The SVO Filter Profile Service, Contributions to the XIV.0 Scientific Meeting (virtual) of the Spanish Astronomical Society, held 13-15 July 2020, Available at: https://www.sea-astronomia.es/reunion-cientifica-2020
Rosich A., Herrero E., Mallonn M., Ribas I., Morales J. C., Perger M., Anglada-Escudé G., Granzer T., 2020, A&A, 641, 16
Sarkar S., Argyriou I., Vandenbussche B., Papageorgiou A., Pascale E., 2018, MNRAS, 481, 2871
Sarkar S., Madhusudhan N., Papageorgiou A., 2020, MNRAS, 491, 378
Savanov I. S., 2019, Astrophysics, 62, 177
Scandariato G., Nascimbeni V., Lanza A. F., Pagano I., Zanmar Sanchez R., Leto G., 2017, A&A, 606, A134
Schlawin E. et al., 2016, PASP, 129, 015001
Silva A. V. R., 2003, ApJ, 585, L147
Silva-Valio A., Lanza A. F., 2011, A&A, 529, A36
Silva-Valio A., Lanza A. F., Alonso R., Barge P., 2010, A&A, 510, A25
Sing D. K. et al., 2011, MNRAS, 416, 1443
Skilling J., 2006, Bayesian Anal., 1, 833
Solanki S. K., 2003, A&AR, 11, 153
Solov'ev A. A., Kirichek E. A., 2019, MNRAS, 482, 5290
Speagle J. S., 2020, MNRAS, 493, 3132
Spruit H. C., 1976, Sol. Phys., 50, 269
Strassmeier K. G., 2009, A&AR, 17, 251
Tinetti G. et al., 2018, Exp. Astron., 46, 135
Tregloan-Reed J. et al., 2015, MNRAS, 450, 1760
Virtanen P. et al., 2020, Nat. Methods, 17, 261
Vogt S. S., 1979, PASP, 91, 616
Vogt S. S., 1981, ApJ, 250, 327
Wakeford H. R. et al., 2019, AJ, 157, 11
Wallace L., Bernath P., Livingston W., Hinkle K., Busler J., Guo B., Zhang K., 1995, Science, 268, 1155
Wing R. F., Spinrad H., Kuhi L. V., 1967, ApJ, 147, 117
Yadav R. K., Gastine T., Christensen U. R., Reiners A., 2015, A&A, 573, A68
Zellem R. T. et al., 2017, ApJ, 844, 27

APPENDIX A: POSTERIOR DISTRIBUTIONS FOR A LOW-OCCULTATION SNR CASE

We here report the corner plot for the low-SNR, white-light transit fit in the scenario with a 14.5 K mag, M star observed with NIRSpec/Prism, and a $T_\bullet = 3200$ K occulted starspot, with $\theta = 0^\circ$, discussed in Section 4.3. In particular, it can be observed that the posterior distribution for the occultation flatness n does not provide enough constraints on such parameter. As a result, a high $\beta_{\rm min}$ is produced, and a warm starspot solution is forced.

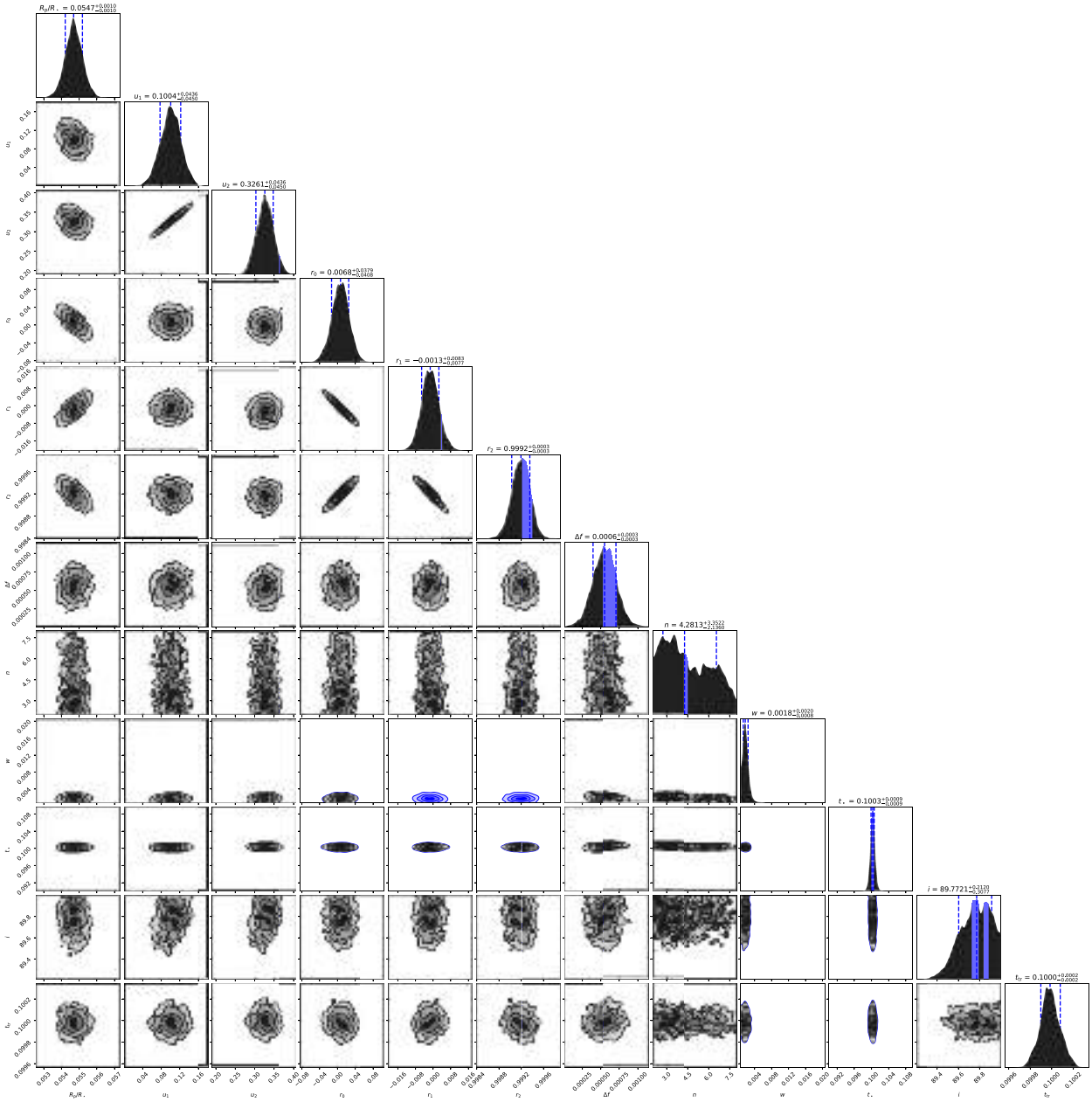

Figure A1. Marginalized posterior distributions for the low-SNR, white-light transit nested sampling on a 14.5 *K* mag, M star observed with NIRSpec/Prism, and a $T_\bullet = 3200$ K occulted starspot, with $\theta = 0^\circ$, as discussed in Section 4.3. The columns represent, from left to right: Planet-to-star radius ratio, linear and quadratic limb darkening coefficient, out-of-transit quadratic trend parameters (r_0, r_1, r_2), flux bump Δf, occultation flatness n, spot width w, occultation time $t_\bullet$, planet orbital inclination, and transit mid-time. On large-SNR occultation cases, the n parameter is tightly constrained.

APPENDIX B: POSTERIOR DISTRIBUTIONS FOR ALL SIMULATIONS

We here provide a version of Figs 5–7 that includes the posterior distributions for all scenarios. The SNR of a given solution represents the baseline for the horizontal histogram of the respective posterior. These plots allow the identification of trends in the bimodality of the solutions, as well as the significance of the 50 per cent percentile values represented in the first version of the figures.

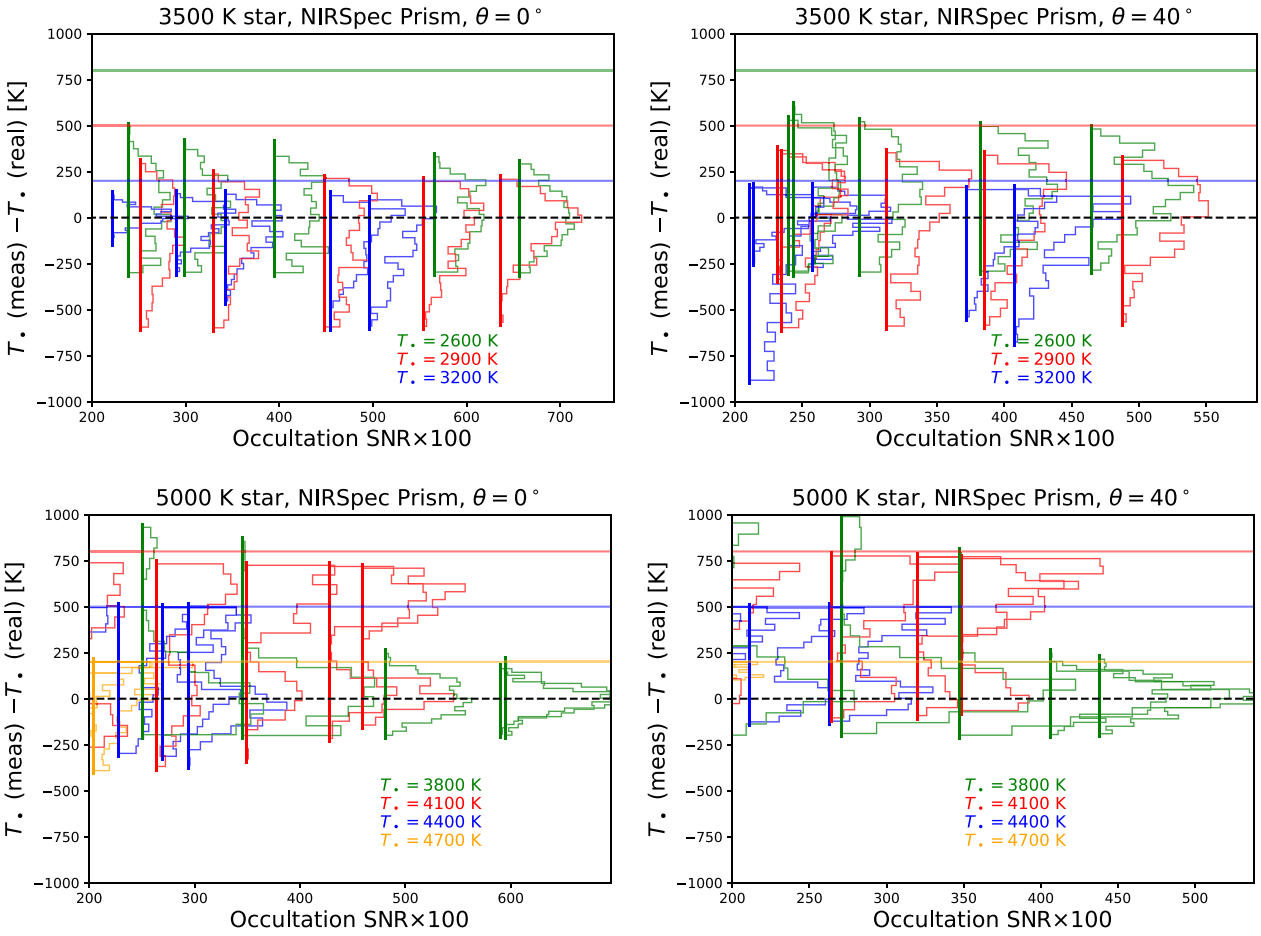

Figure B1. Posterior distributions of the difference between the measured and the true $T_\bullet$ for the simulations carried out for NIRSpec/Prism, as a function of the occultation SNR multiplied for visualization purposes. The figures are divided by stellar temperature (rows) and starspot limb-angle (column). The baseline of each horizontal histogram indicates the SNR of the corresponding scenario and the probability in the distributions increases along the x-axis (different probability values in a given histogram are all related to the same SNR value). Different colours represent different true $T_\bullet$ cases, and stellar $T_\star - 100$ K values (the lowest allowed in our $T_\bullet$ fit) are marked with horizontal lines with the corresponding colour for each scenario. Bimodal distributions for the K star, 4100 K starspot, mid- to low-SNR case can be clearly distinguished; in the lowest SNR cases, only a lower limit can be assigned to $T_\bullet$.

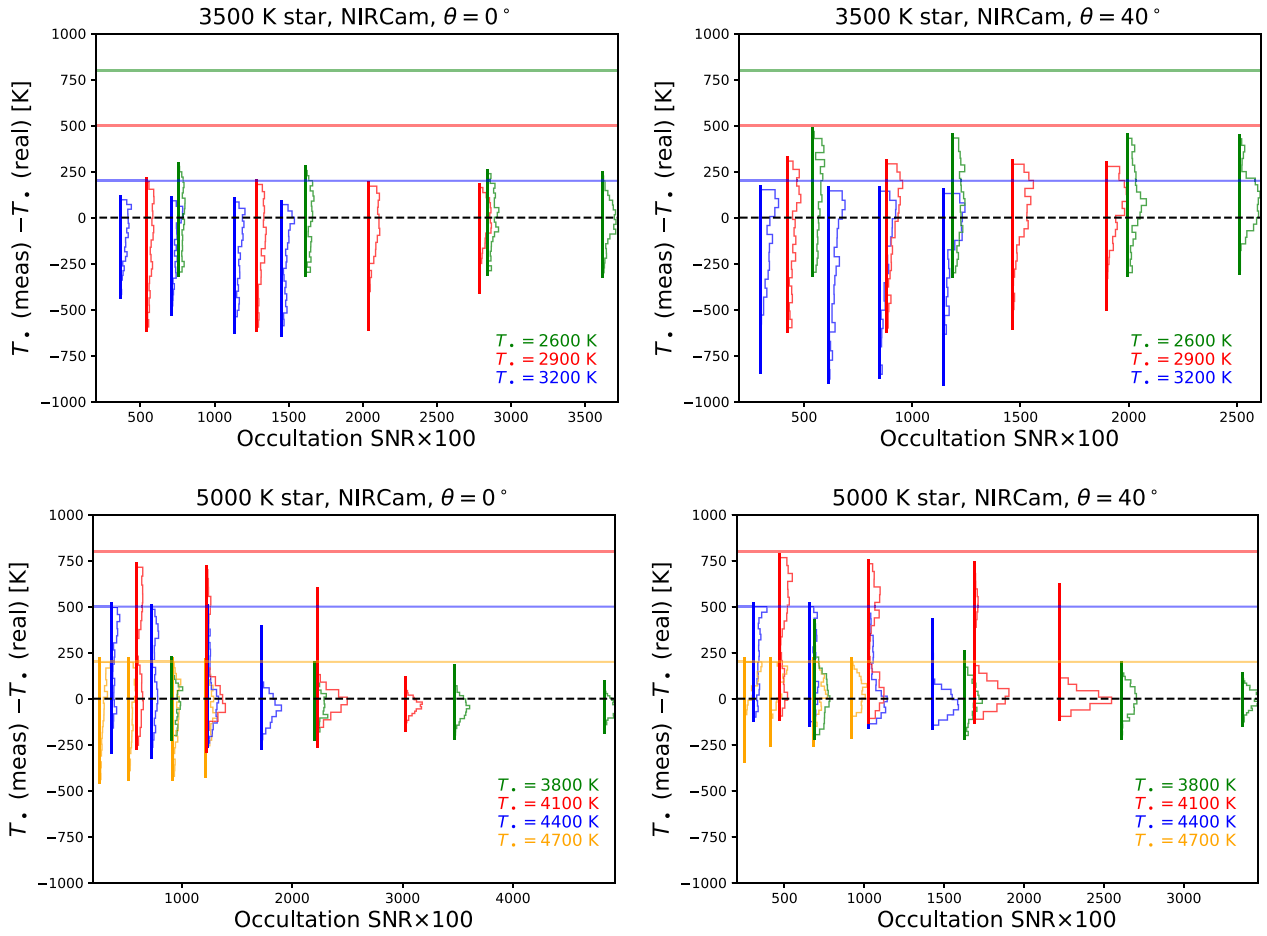

Figure B2. Same as Fig. B1, but for NIRCam/F150W2 + F322W2.

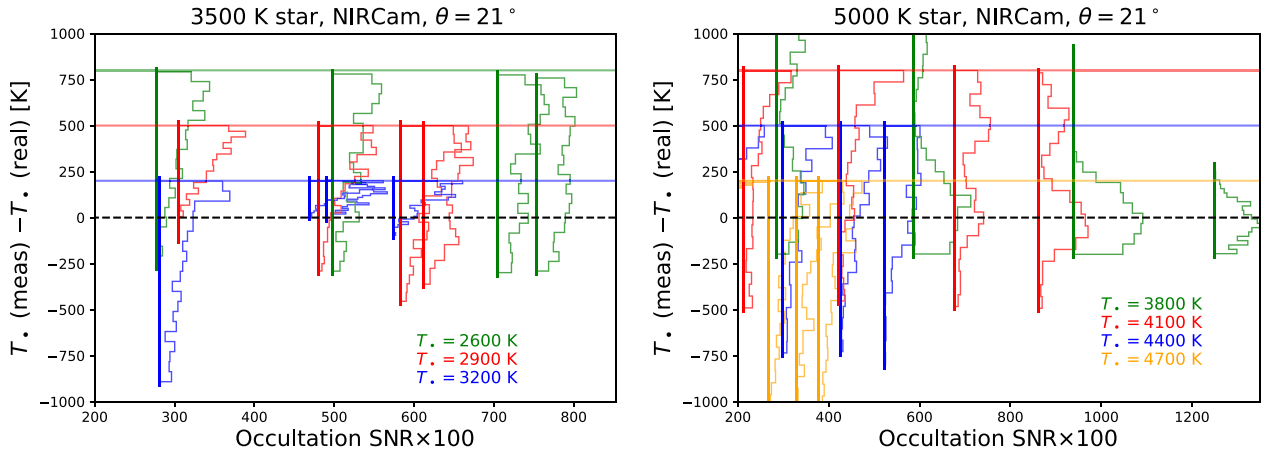

Figure B3. Same as Fig. B1 for spots at 21° stellar latitude, for the M (left) and K (right) scenarios observed by NIRCam/F150W2 + F322W2.

This paper has been typeset from a TEX/LATEX file prepared by the author.